Article

Pathological cardiolipin-promoted membrane hemifusion stiffens pulmonary surfactant membranes

Marilyn Porras-Gómez,[1] Tooba Shoaib,[1] Dylan Steer,[1] Rosa Maria Espinosa-Marzal,[2] and Cecília Leal[1,*]

[1]Department of Materials Science and Engineering, University of Illinois Urbana-Champaign, Urbana, Illinois and [2]Department of Civil and Environmental Engineering, University of Illinois Urbana-Champaign, Urbana, Illinois

ABSTRACT   Lower tract respiratory diseases such as pneumonia are pervasive, affecting millions of people every year. The stability of the air/water interface in alveoli and the mechanical performance during the breathing cycle are regulated by the structural and elastic properties of pulmonary surfactant membranes (PSMs). Respiratory dysfunctions and pathologies often result in, or are caused by, impairment of the PSMs. However, a gap remains between our knowledge of the etiology of lung diseases and the fundamental properties of PSMs. For example, bacterial pneumonia in humans and mice has been associated with aberrant levels of cardiolipin, a mitochondrial-specific, highly unsaturated 4-tailed anionic phospholipid, in lung fluid, which likely disrupts the structural and mechanical integrity of PSMs. Specifically, cardiolipin is expected to significantly alter PSM elasticity due to its intrinsic molecular properties favoring membrane folding away from a flat configuration. In this paper, we investigate the structural and mechanical properties of the lipidic components of PSMs using lipid-based models as well as bovine extracts affected by the addition of pathological cardiolipin levels. Specifically, using a combination of optical and atomic force microscopy with a surface force apparatus, we demonstrate that cardiolipin strongly promotes hemifusion of PSMs and that these local membrane contacts propagate at larger scales, resulting in global stiffening of lung membranes.

SIGNIFICANCE   Bacterial pneumonia, whether it is primary or acquired after other superimposed pulmonary infections (such as in COVID-19 patients), is the most pervasive lower respiratory tract infection. Pneumonia alters the lipid composition of pulmonary surfactant membranes. We know that cardiolipin, a mitochondrial-specific lipid, is significantly elevated in mammalian lungs suffering from pneumonia. However, we know much less about the implications that cardiolipin has on pulmonary membrane biophysical properties. In this work, we investigate the effect of cardiolipin in the structure and elasticity of pulmonary membranes. We observe that cardiolipin induces loss of elasticity of the membranes due to hemifusion of apposed monolayers. This paper underpins how the biophysical properties of pulmonary membranes impart the etiology of pneumonia-like conditions.

INTRODUCTION

Pulmonary surfactant membranes (PSMs) are surface-tension-lowering materials composed of a lipo-protein monolayer at the air-water interface and multilayer mesostructures in the aqueous hypophase of the alveoli. Phosphatidylcholines (PCs) are the most abundant phospholipids in the lung surfactant, comprising about 70% by mass, followed by phosphatidylglycerols (PGs; up to 10% by mass). Among the PCs, dipalmitoylphosphatidylcholine (DPPC) predominates, making up 40% by mass of PCs [1–3]. Saturated PCs form tightly packed films capable of reducing the surface tension to <1 mN/m at physiological temperature. However, PCs adsorb poorly at the air-water interface. Adsorption is significantly improved by other phospholipids, such as unsaturated PGs, and by the assistance of surfactant proteins [4]. Alveolar interfacial stability and mechanical performance is regulated by PSMs' elastic properties, and it has been postulated that their impairment is associated with respiratory dysfunctions and pathologies [5].

A minor lipid component of PSMs (1%–2% of total phospholipids) is cardiolipin (CL), a highly unsaturated anionic phospholipid. Aberrant amounts of CL in mammalian

alveoli have been associated with the etiology of lung diseases such as pneumonia (6,7). When introduced artificially to healthy lungs (5–15 mol %), CL induces pneumonia-like symptoms and disrupts lung surfactant function (7). In addition, overexpression of Atp8B1, a lipid-pump transporter that clears out CL from the PSMs, restores lung function after experimentally induced pneumonia (7).

Unlike other phospholipids, CL has two phosphatidic acids linked together by a glycerol bridge, which each contain two acyl chains, resulting in a large 4-tailed lipid molecule with a relatively small anionic headgroup. This chemical structure results in an inverted-conical molecular shape favoring the self-assembly of lipid monolayers with negative curvature $C<0$ (9,10) The terms cone and inverted cone have been used interchangeably to refer to the same molecular shape. Hence, spontaneous curvature or packing parameter are the preferred terms to describe molecular geometry. Lipid molecular shape is best described by the Israelachvili's packing parameter $P = \nu/(a_0 l_c)$ (8), where ν is the volume of the hydrocarbon chains, a_0 s the effective area per headgroup, and l_c is the chain length. In this article, an inverted-conical shape refers to lipid molecules with small headgroups relative to the hydrocarbon tails ($P > 1$). A monolayer formed with a collection of lipids of a given shape has an associated spontaneous curvature (C_0). Lipid species like CL are described as $C_0<0, P>1$, preferentially localizing at highly negatively curved membrane portions (9), such as in microdomains in mitochondrial and rod-shaped bacterial membranes (11). Notably, lipid sorting according to curvature is not only regulated by molecular shape, since lipid-lipid and lipid-protein interactions provide alternatives to lower the energy barrier of curvature-driven lipid sorting (9,12).

The inclusion of CL in PSMs is likely to affect their curvature and general elastic properties, which should in turn affect their mechanical behavior and functional ability to expand and contract during the breathing cycle. In our previous work, we found that increased levels of CL and calcium ions cause dehydration of model and bovine-extracted PSMs and enhance the formation of phase-separated domains (13). Later on, we found that CL promotes the formation of local intermembrane contacts in the PSMs, altering oxygen permeation (14). However, the microscopic understanding of how CL disrupts PSM function and mechanical properties and how to ameliorate them remain unknown.

In this paper, we employ atomic force microscopy (AFM) topography combined with fast force mapping, surface force apparatus (SFA), and confocal microscopy to show that CL restricts the elasticity of model and bovine-extracted PSMs and promotes phase separation. Interestingly, CL dramatically decreases the energetic barrier for membrane fusion leading to the quick (20 s) formation of hemifusion membrane contacts at intermembrane separations as large as 12 nm. These membrane contacts significantly stiffen the

PSMs by at least 10 MPa in Young's modulus. We postulate that these factors collectively impair PSM mechanical function and contribute to the etiology of lung respiratory diseases.

MATERIALS AND METHODS

Materials

The lipids 1,2-dipalmitoyl-sn-glycero-3-phosphocholine (DPPC), 1,2-dioleoyl-sn-glycero-3-phospho-(1′-rac-glycerol) (sodium salt) (dioleoylphosphatidylglycerol [DOPG]), and 1,3-bis(sn-3′-phosphatidyl)-sn-glycerol (heart, bovine [sodium salt] CL) were purchased from Avanti Polar Lipids (Alabaster, AL) and suspended in chloroform, with each one at a concentration of 25 mg/mL. The lipid model is composed of DPPC:DOPG 3:1 (molar ratio) when mimicking healthy PSMs and the same ratio of DPPC:DOPG with 8 mol % CL when mimicking diseased PSMs. The bovine PSMs are extracted from bovine lung surfactant, where the manufacturing process removes hydrophilic proteins, the majority of which is SP-A, and selects for hydrophobic phospholipids and SP-B and SP-C. BLES Biochemicals (Ontario, Canada) kindly provided the bovine extract BLES as a dry film. The bovine extract was dissolved in chloroform, and to mimic diseased bovine PSMs, 8 mol % CL was added. Fluorescent probe 1,1′-dioctadecyl-3,3,3′,3′-tetramethylindocarbocyanine perchlorate was purchased from Thermo Fisher Scientific (Waltham, MA).

AFM, force mapping, and force curve analysis

For the preparation of supported lipid multilayered (SLM) membranes, stock solutions of lipids in chloroform were mixed to a final concentration of 25 mM. The bovine PSM extract was suspended in chloroform at a concentration of 25 mg/mL. SiO_2 substrates of 1.5 cm^2 were washed with an organic solvent, followed by sonication in an ultrasonic bath for 10 min, and they were then dried with a nitrogen flow. A volume of 100 μL lipid or bovine extract solutions was pipetted onto each clean SiO_2 substrate, which, afterward, was immediately accelerated to 3,000 RPM for 30 s using a spin coater (VTC-100A, MTI, Richmond, CA). The samples were vacuum dried for at least 2 h. SLM samples were scanned in air afterward. For the preparation of supported lipid bilayers (SLBs), stock solutions of lipids in chloroform were mixed. Subsequently, the chloroform was evaporated under nitrogen gas flow until dry, followed by being kept under vacuum for at least 2 h. The resultant dry lipid film was then resuspended in 3 mol % $CaCl_2$/deionized water (18.2 M Ω/cm, Millipore, Darmstadt, Germany) to reach a final concentration of 1 mM of lipids. This solution was gently mixed and afterward kept at 4°C to allow swelling for 1 h. To obtain small unilamellar vesicles (SUVs), the solution was then sonicated in an ultrasonic bath for 30 min and, finally, extruded 11 times each through 0.2 and then 0.1 μm pore-size polycarbonate membranes on an extruder (Avanti Polar Lipids) before analysis. The SUV solution was used immediately or stored at 4°C until needed. For the vesicle fusion, 2 mL SUV suspension was pipetted onto clean SiO_2 substrates, which were then heated at 60°C for 45 min. After slowly cooling down the system to room temperature, SiO_2 substrates were carefully rinsed with deionized water to remove the SUV excess. Substrates were mounted onto the AFM while avoiding dewetting. Finally, 100 μL deionized water was carefully pipetted on the sample surface and incubated for 20–30 min before scanning. All AFM experiments were performed in a high-speed Cypher AFM (Asylum Research-Oxford Instruments, California, USA). Topography and phase imaging were performed in intermittent contact (tapping mode) in air using Si_3N_4 cantilevers (BL-AC40TS, Oxford Instruments, Santa Barbara, CA). The nominal curvature radius of the tips is 8 nm, and the length, width, and thickness of the cantilevers are 38, 16, and 0.2 μm, respectively, with a nominal spring constant of 90 pN/m (values were in the range of 80–110 pN/m). The height and phase signals were collected simultaneously

in both trace and retrace directions. From SLBs, we calculated the bilayer thickness, D_B, by measuring 8 cross-section lines of 3 different AFM images giving $n = 24$ per sample (healthy and diseased PSM lipid models). We calculated surface roughness Sq using the discrete approximation of the root mean-square (Eq. S1) in the Asylum Research software v.16 supported in Igor Pro v.6 (www.wavemetrics.com). We used SLM topography images of areas of 25 μm^2 and resolution of 512 × 512 data points (Fig. S1; Table S1). For the fast-force-mapping experiments, the cantilever spring constant and the resonance frequency were calibrated using the thermal spectrum before each experiment. The amplitude sensitivity (nm/V) was calibrated in air in all cases and also in fluid when mapping SLBs. The force applied to the membranes was fixed to the lowest possible value allowing reproducible mapping (1 V corresponding to a force range of 200–400 pN). The scan rate was set to 100 Hz on an area of either 5 × 5 or 10 × 10 μm. The total z-piezo (vertical) displacement was set to 200 nm. Generally, force maps comprised 128 points × 128 lines resulting in 16,384 data points per map (Table S2). Force maps were processed using the accompanying Asylum Research software v.16. All reported Young's modulus E values result from the peak of a Gaussian fit of the elasticity distribution obtained from the respective force maps. The approximate value of E was calculated from the approaching curves by using the Hertz model for conical tips (Sneddon model) (Eq. S2; Fig S2).

SFA

Stock solutions of lipids in chloroform were mixed. Subsequently, the chloroform was evaporated under nitrogen gas flow until dry, followed by being kept under vacuum for at least 2 h. The resultant dry lipid film was then re-suspended in deionized water to reach a final concentration of 10 mM and was kept for 1 h at 4°C. Lipid solutions were diluted to a concentration of 0.15 mM. The samples for SFA were sonicated for 30 min and extruded 11 times each through 0.2 and then 0.1 μm pore-size polycarbonate membranes on an extruder (Avanti Polar Lipids) before analysis. Freshly cleaved (atomically smooth) mica sheets were used as substrates. The sheets were back-silvered and glued onto cylindrical-shaped glass lenses and mounted in the fluid cell in a cross-cylinder geometry. When white light passes through the surfaces, it is reflected multiple times in the silver layers, providing an interference pattern known as fringes of equal chromatic order. Analyzing the interference by multiple beam interferometry yields the absolute mica–mica distance (D) between the surfaces with sub-angstrom resolution. This happens in the extended SFA in real time via a numeric algorithm called fast spectral correlation (15,16). We used SFA to measure the forces between bilayers in water close to neutral pH (6.84) at 25°C, while one surface is driven toward the other (approach or loading) and apart from each other (separation or unloading) at 0.1 nm/s to achieve quasi equilibrium. The force between the opposing surfaces (F) is measured via the deflection of the double cantilever spring, which is attached to one of the lenses. The deflection of the spring is determined via the change in D, and by applying Hooke's law, the force is calculated as a function of D or the distance between bilayers, D_B. In units of surface energy, the resolution of the SFA is ≈ 0.01 mJ/m^2, and the distance measurement has a precision of 30 pm.

Laser scanning confocal microscopy

Samples were prepared following the papyrus method (17). Plain bovine PSM extract (healthy) and with 8 mol % of CL (diseased) were individually mixed with 0.1 mol % of 1,1′-dioctadecyl-3,3,3′,3′-tetramethylindocarbocyanine perchlorate in chloroform at a concentration of 5 mg/ml. A volume of 50 μL of each lipid solution was pipetted onto pieces of paper (1 cm in diameter, Whatman Grade 1). The chloroform was evaporated under nitrogen gas flow until dry, followed by being kept under vacuum overnight protected from light exposure. The samples were hydrated with 700 μL 100 mM sucrose/deionized water and incubated in the dark for 2 h at

60°C. Samples were slowly cooled by turning off the incubator and leaving the samples inside. The filter paper was swirled around in the sucrose solution to detach the vesicles, and the solution was transferred into Eppendorf tubes for storage. Imaging was performed within 2 days. Vesicles were slowly transferred into an 8-well chamber slide (Nunc Lab-Tek) filled with 200 μL 100 mM glucose for imaging on an LSM 800 confocal microscope (Carl Zeiss Microimaging, Jena, Germany), with a Plan-Apochromat 63×/1.40 Oil M27 objective lens.

RESULTS AND DISCUSSION

We evaluated how CL affects the elasticity and bilayer fusion forces of PSMs using a lipid-based model and a bovine lung surfactant extract. The lipid model consists of a mixture of DPPC and DOPG at a molar ratio of 3:1 (healthy PSM model). We compared them against CL-containing mixtures (8 mol %) to mimic PSMs exposed to aberrant CL levels, as experimentally observed in diseased lungs (7). We characterized these systems using AFM topography and fast force mapping via the study of SLM films adsorbed onto SiO$_2$ substrates exposed to high relative humidity (85%–90%) environments. This platform captures the crowded viscous (low free water) environment that PSMs operate in. We also performed AFM measurements on SLBs in fluid for comparison. In addition, we studied mica-SLBs of the PSM models using SFA. Finally, we studied bovine PSM extracts in bulk (vesicles in water) with confocal microscopy.

CL induces phase-separation of PSMs

Fig. 1 shows AFM scans of lipidic model PSMs (DPPC: DOPG 3:1 molar ratio) in the form of deposited multilayered films in equilibrium with high air humidity mimicking healthy and diseased (with CL) PSMs. AFM scans small areas of the surface of the sample with a sharp tip providing the advantage of resolving 3D features in the topography maps while simultaneously yielding phase-contrast maps that convey information of the viscoelastic differences in the material. AFM topography maps are analyzed to calculate areal surface roughness parameters such as Sq (root mean square roughness). Healthy PSMs displayed a relatively more homogeneous topography with a Sq of 4.9 ± 0.4 nm compared with model diseased PSMs (containing CL) with a Sq of 7.7 ± 0.4 nm. Additional data are provided in Fig. S1 and Table S1. Also, CL-containing PSMs exhibited domain-like structures thicker than their surroundings (Figs. 1 A and B).

The differences observed in the topography maps overlap with angle variations in the phase maps (Fig. 1 C). Intermittent contact (or tapping mode) uses the amplitude of cantilever oscillation to detect changes in the tip-sample interaction forces, which translate to the topography image. The phase shift of the tip response is recorded in parallel to the topography. A lag in the oscillation of the cantilever (i.e., phase shift) correlates to the composition and viscoelastic
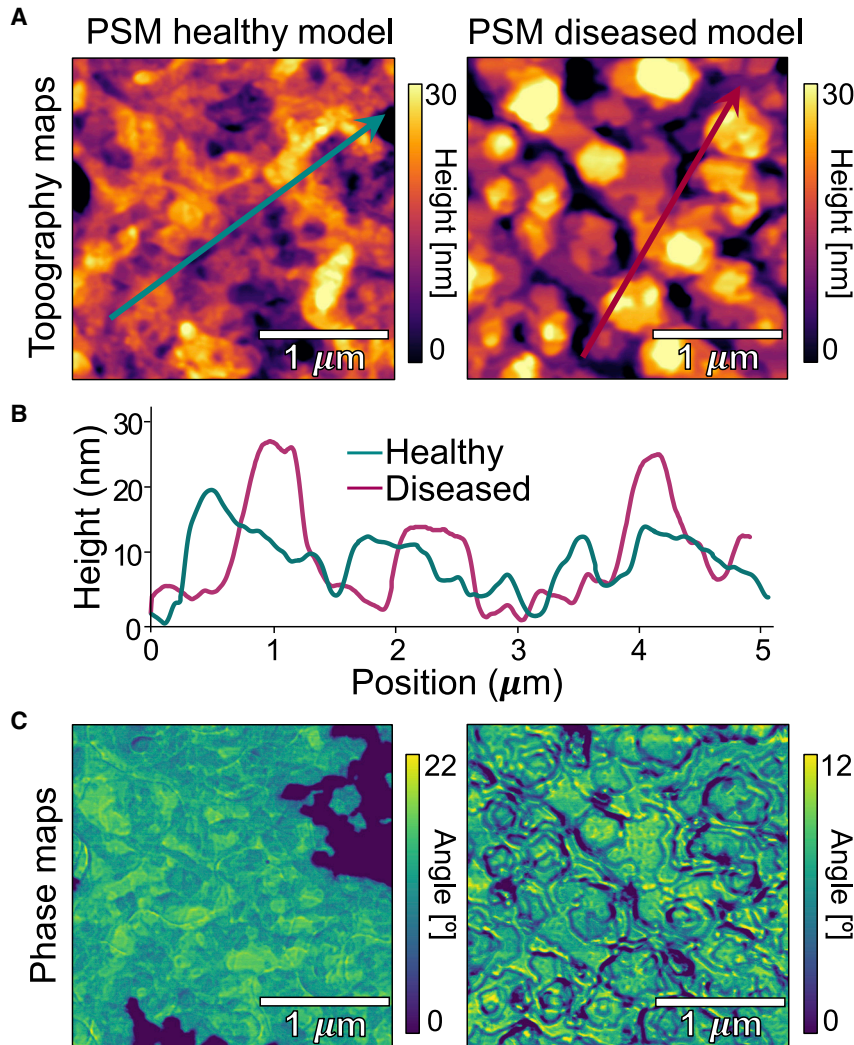
A

Topography maps

PSM healthy model

PSM diseased model

B

C

Phase maps

FIGURE 1 AFM images of PSM model systems of lipid multilayers adsorbed onto SiO_3, equilibrated at room temperature, and with high RH (85%–90%). (*A*) Topography maps of healthy (DPPC:DOPG 3:1 molar ratio with no CL) and diseased PSMs (DPPC:DOPG 3:1 molar ratio with 8% mol CL). (*B*) Section profiles as indicated by the lines in (*A*). (*C*) Phase maps corresponding to the same area scanned in the topography maps in (*A*). To see this figure in color, go online.

properties of the material, which are registered as bright and dark regions in phase maps (18). Hence, phase mapping characterizes spatial variations of mechanical properties of phase-separated materials such as certain lipid mixtures. The AFM results indicate two main findings along these lines. First, healthy model PSMs exhibit a more homogeneous phase across larger areas. Because of poor miscibility of saturated and unsaturated lipids, darker patches (lower angle) likely correspond to DPPC-rich areas (gel phase, L_β), whereas lighter areas (yellow) likely correspond to DOPG-rich areas (fluid phase, L_α). Moreover, both lipids also coexist in the mixture (green areas) (Figs. 1 *C* and S1). Second, the diseased PSM model exhibits a domain-like structure formation visible in the height map (Fig. 1 *A*) that is also readily observable in the phase map (Fig. 1 *C*). Both models display signatures of phase separation. Previous work (13) showed that lipid models of PSMs composed of DPPC:DOPG mixtures phase separate in DPPC (saturated)-rich and DOPG (unsaturated)-rich domains in multilamellar bodies. Evidence of gel/fluid domain

formation in CL-DPPC monolayers has been reported using AFM (19). Remarkably, in this system, the addition of CL further induced phase separation and domain registration, i.e., phase-like (gel or fluid) domains aligned in registry in the normal direction across the multilayer thickness (13). Here, we study this behavior with AFM and resolve CL-induced bilayer domains that couple across several layers of the multilamellar-deposited PSMs (Fig. 1). We have reported (13) that high concentrations of Ca^{+2} (up to 12 mM) affect the order and dynamics of DPPC:DOPG model PSMs. Ca^{+2} induces an expected decrease in inter-membrane separation but only when CL is absent, and when CL is present, the average intermembrane separation increases with Ca^{+2} addition. It is noteworthy that this lipid system is at the cusp of phase separation even without any Ca^{+2}, as the results here suggest phase separation in PSM models without Ca^{+2}.

In addition, we calculated the bilayer thickness, D_B, to be 8.0 and 6.8 nm for healthy and diseased PSM models, respectively, from AFM cross-section analysis (Fig. S3).
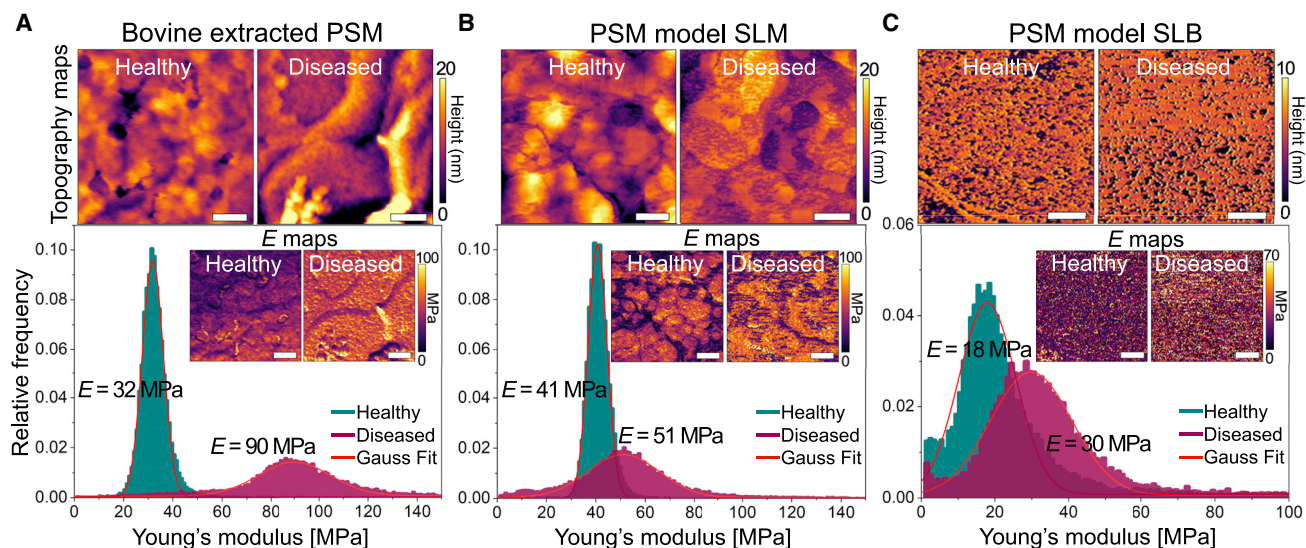
FIGURE 2   AFM force mapping analysis of PSMs. (A–C) Topography maps and Young's modulus E distributions with insets of elasticity maps of (A) healthy and diseased bovine-extracted PSMs at 85%–90% RH, (B) healthy and diseased PSM model supported lipid multilayers (SLMs) at 85%–90% RH, and (C) healthy and diseased PSM model supported lipid bilayers (SLBs) in water. Scale bars correspond to 200 nm in (A) and (B) and to 1 μm in (C). To see this figure in color, go online.

We calculated the thickness of SLM films (14) to be 107 ± 10 and 80 ± 2 nm for healthy and diseased PSM models, respectively, using the AFM tip-scratch method. Hence, we estimate that PSM films are made of 12 or 13 bilayers stacked up. Polyunsaturated CL tends to spread out its hydrocarbon chains, resulting in a larger area per lipid compared with saturated phospholipids (20). As a result, the introduction of CL is likely to induce some bilayer and film thinning.

CL stiffens PSMs

AFM phase mapping distinguishes local differences in mechanical properties but gives qualitative data only. More recently, the capability of fast force mapping has been incorporated into AFM, in which the maps quantitatively reflect the mechanical properties such as elasticity and adhesion of planar membranes. We applied AFM fast force mapping to obtain elasticity maps with Young's modulus E distributions as a means to examine the effect of CL on the elasticity of PSMs in different forms. Young's modulus is an intensive property that characterizes a material independently of its geometry. Specifically, we evaluated SLMs of 1) bovine-extracted PSMs and 2) a PSM model comprising a DPPC:DOPG 3:1 molar ratio both adsorbed onto SiO_2 at ambient temperature and high relative humidity (85–90%), as well as 3) SLBs comprising DPPC:DOPG (3:1 mol:mol) in water. We compared all systems with and without CL inclusion (8 mol %). Despite the intrinsic viscoelastic behavior of the membranes, the Hertz elastic model fits the response to small loads relatively well, yielding the average E with appropriate precision (details provided in Sections S2 and

S3 in the supporting material). This has been observed previously for other membrane systems (21–23).

The addition of CL to the different PSM forms (bovine-extracted SLM, model SLM, and model SLB) significantly affects their elasticity. The average E of healthy bovine PSM extracts is 32 MPa. The addition of CL leads to a 3-fold increase in E (90 MPa) (Fig. 2 A). In addition, CL-loaded bovine PSM extracts exhibit a wider distribution of E compared with the narrow peak obtained for native bovine PSM extracts. The addition of CL also results in stiffer SLMs and SLBs of PSM models. SLMs yield a value of E equal to 41 MPa without CL and 51 MPa with while also widening the distribution of E (Fig. 2 B). SLBs are generally softer (Fig. 2 C) but exhibit a raise in average E from 18 to 30 MPa upon CL addition. In all cases, CL-loaded PSMs display wider Young's modulus distributions (Table S2). This observation is consistent with the fact that CL expands the phase (L_α-L_β)-separation domains in DOPG:DPPC membranes, which results in widespread lateral heterogeneity of membrane stiffness.

We estimated the stretch (K_A) and bending (κ_C) moduli with the AFM force map data using the following equations (24): $K_A = ED_B/(1 - \nu^2)$, $\kappa_C = ED_B^3/24(1 - \nu^2)$, where D_B is the bilayer thickness, here estimated to be 8.0 and 6.8 nm for healthy and diseased PSM models, respectively, from AFM topography (Fig. S3), and ν is the Poisson ratio of lipids, $\nu = 0.5$. All PSM samples containing CL (diseased) exhibited larger moduli (Table S3), which is consistent with the fact that the addition of CL restricts the mechanical deformability of PSMs. Adding CL to bovine PSM extracts results in an almost 3-fold increase in κ_C (160–450 k_BT). In the PSM SLM systems, CL induces an increase in κ_C from 205 to 255 k_BT. SLB PSMs evolves

from $\kappa_C = 90$ to $150\,\mathrm{k_B}T$ upon CL addition. A similar trend is observed in the K_A modulus (Table S3). The latter indicates that CL increases the resistance of PSMs to deform (stretching and bending). Similarly, using X-ray scattering, a study reported that CL stiffened dimyristoylphosphatidylcholine, well-aligned membranes in the fluid phase, reporting a 50% increase in κ_C from 13 to 19 $\mathrm{k_B}T$ with small amounts of CL (25).

Membrane additives often alter membrane elasticity. For instance, addition of hydrophobic C_{60} fullerenes affect the mechanical resistance of PC lipid bilayers. Young's modulus measured with AFM of SLBs increases in the gel phase from $E = 42$ to $E = 69$ MPa (26). It is postulated that C_{60} alters the orientation of the hydrocarbon tails, increasing the cohesion of the hydrophobic part of the bilayer and the van der Waals attraction force. Similarly, CL, a highly hydrophobic phospholipid (four hydrocarbon chains), likely changes the intra-chain configuration and inter-chain orientation of the hydrocarbon tails, leading to stiffening of the PSM SLBs. Moreover, the addition of cholesterol (hydrophobic molecule) to membranes leads to a stiffening of the "fluid" areas and a softening of the more "rigid" domains (27). The addition of physiological amounts of cholesterol (10–20 mol %) to bovine PSM extracts does not impair the membrane's surface activity; even more, cholesterol leads to the formation of liquid-ordered L_o phases, which slightly improves it. Conversely, supraphysiological levels (50 mol %) of cholesterol induce structural changes in the membrane (formation of L_d phases) and significantly decrease its ability to lower surface tension (28). In addition, previous AFM work has shown that an excess of cholesterol (40 mol %) in bovine PSMs may stiffen certain fluid areas of the membrane (29). We preliminarily tested the effect of cholesterol on the lipid PSM model. The addition of physiological levels of cholesterol (15 mol %) stiffened the healthy PSM model from 41 to 58 MPa (Fig. S4). This loss of elasticity induced by cholesterol might not be enough to impair surface activity. Nevertheless, further investigation is required to elucidate the effects of cholesterol at physiological and excessive concentrations, especially when combined with CL in diseased PSMs.

The addition of CL to membranes affects the local order and dynamics of the host membrane (30, 31), and CL-containing membranes are structurally more compact (32). For instance, the movement of lipids is slower due to the restrictive nature of CL large molecules in CL-rich membranes such as the inner mitochondrial membrane, thus slowing the diffusion in the plane parallel to the membrane (33). We previously found that CL induces significant dehydration of lung multilamellar vesicles (13). Upon dehydration, two apposed bilayers are brought into close contact, eventually leading to the merging of the proximal monolayers. The resulting structure is a stalk that, in turn, expands into hemifusion (34). The formation of stalks and hemifused contacts is likely stabilized and regulated by surfactant proteins in the alveoli (35). Despite the latter, stalk formation mediated by CL has been reported in protein-free model PSMs (14). Here, we propose that healthy PSMs appear softer because they are composed of mostly discrete, unconnected membranes separated and cushioned by water layers, whereas diseased CL-laden PSM SLMs are interconnected by stalks and hemifused hydrophobic contacts, leading to membranes with higher Young's modulus. We have shown that excessive hydrophobic membrane contacts disrupt oxygen flow in PSMs (14). This structural change, combined with PSM stiffening, is likely to affect not only their mechanical functions during breathing but also protein binding and partition, all likely to impart pathological lung conditions.

CL enhances hydrophobic interaction and bilayer hemifusion

To further investigate the effect of CL on PSM interconnection and hemifusion, we measured the forces between PSM bilayers using the SFA (36). We also measured inter- and intra-membrane adhesion and hemifusion characteristics. The SFA has been used to study hemifusion of mica- and polymer-SLBs as a function of temperature (37), lipid phase and composition (37–39), Ca^{+2} concentration (40), and pressure (41) as well as the behavior of biomolecules, like tau dimers and glycoproteins (42,43).

Fig. 3 shows SFA data obtained for model PSMs comprised of DPPC:DOPG (3:1 molar ratio) with and without CL to mimic diseased and healthy states, respectively. Vesicles in water of model PSMs adsorbed to mica surfaces. CL-containing vesicles underwent spontaneous rupture on mica in less than 1 hour and formed lipid bilayers with $D_B \approx 6$ nm. The measurements of adsorption of the healthy vesicles on mica showed that spontaneous rupture did not occur. We obtained surface forces (Fig. 3 A) between healthy vesicles (blue) and diseased SLBs (red and orange). The interaction potential was fit to the inter-bilayer forces of the diseased model (Eq. S3). The method to fit the model to the experimental results is described in detail in Section S7 of the supporting material. In brief, the long-range force for the diseased-model vesicles is of electrostatic origin and, hence, modeled according to Debye-Hückel theory (8) with a Debye length λ_{EDL} that agrees well with the solution concentration. This provides a surface potential of -106 ± 25 mV. The required number of dissociated CL molecules to reach this surface potential is estimated via the Grahame equation (8), and it is $\approx 17\% \pm 2\%$, considering that CL has two negative charges.

The onset of an attractive interaction leading to the interconnection or the hemifusion of PSM SLBs is found at a separation of 12 nm, as reflected by the jump in of the surfaces (arrows in Fig. 3 B). This attractive interaction at a range of inter-bilayer separation $D = 12$ nm cannot be justified by van der Waals forces, but it is possibly due to an
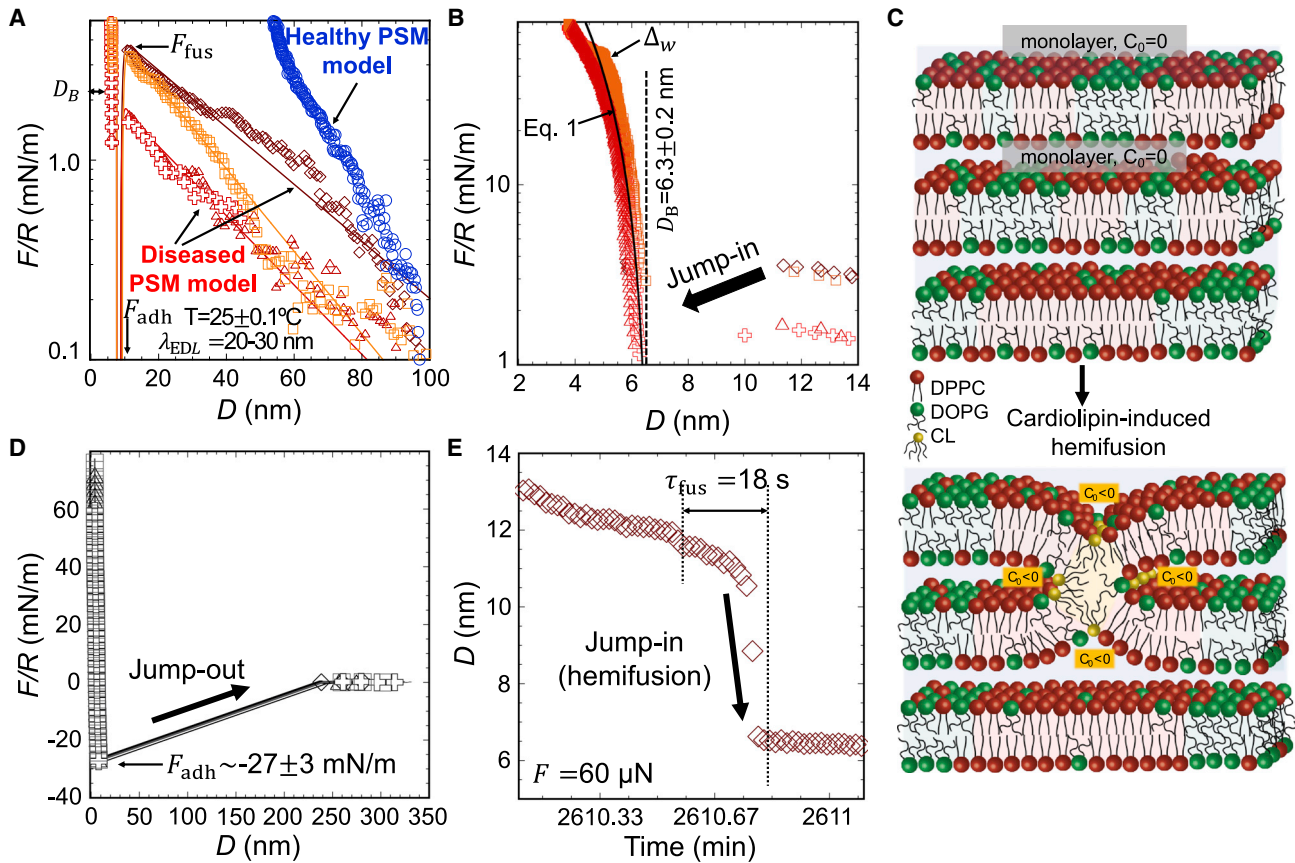
FIGURE 3   SFA analysis of CL-induced hemifusion contacts formation on PSM model (DPPC:DOPG 3:1 mol % with [diseased] and without [healthy] CL) mica-SLBs in water at room temperature. (A) Long-range force (F) versus (D). Lines are fits of Eq. S3 to experimental data (red-orange for inter-bilayer forces and blue for inter-vesicles forces). (B) Short-range inter-bilayer forces; line is the fit of Eq. 1 to experiment. (C) Schematic of the PSM model highlighting two juxtaposed monolayers that join through hemifusion mediated by inverted-conical CL molecules. (D) Force profile during separation (jump out) of bilayer leaflets. (E) Time-resolved hemifusion (jump in) at an applied compression of 60 nN. To see this figure in color, go online.

interaction potential of hydrophobic nature, as described by Eq. S3. We propose that PSM SLBs hemifuse by a mechanism proposed by Helm et al. (39,44) in which bilayer stresses result in a localized spreading of molecules, causing exposure of the hydrophobic interior (Fig. 3 C). The hemifusion barrier is the maximum force before the jump in happens. In the experiments, the hemifusion energy barrier is small ($F_{fus} = 2 \pm 1$ mJ/m^2; see F_{fus} in Fig. 3 A) compared with the reported results for other phospholipid bilayers (45). A compression up to 100 mN/m does not lead to vesicle fusion in the absence of CL (Fig. S5), indicating that the membrane-fusion energy is much higher. The presence of CL likely lowers the energy barrier for hemifusion because of its high hydrophobicity, with four tails. The fit of Eq. S3 to the experimental data provides an interfacial tension (γ) between 23 and 41 mJ/m^2, increasing with the compression applied before jump in, as the exposed hydrophobic area increases. The model predicts an adhesive minimum, which agrees well with experimental results, $F_{adh} \approx 27 \pm 3$ mN/m (Fig. 3 D). This force is converted into adhesion energy using the Johnson–Kendall–Roberts model, $W_{adh} = -5.7 \pm 0.6$ mJ/m^2. The estimated adhesion

energy W_{adh} characterizes the inter-leaflet hydrophobic interaction.

The real-time measurements show that hemifusion between discrete bilayers takes less than 20 s at the center of contact area (Fig. 3 E). This is much faster than reported times for the hemifusion of mixed bilayers of 1,2-dioleoyl-sn-glycero-3-phosphocholine, brain sphingomyelin, and cholesterol (1:1:1 molar ratio) in similar SFA experiments (2.5–19 h) (41) but is closer to *in vivo* times (46). Perhaps the electrostatic repulsion provided by CL reduces lipid packing and facilitates lipid rearrangements, despite the cohesive strength between the tails. Nevertheless, further investigation is needed to dissect the different effects of CL, e.g., via the screening of electrostatic interactions through an increase in ionic strength.

The compressive (bulk) modulus B of the PSMs was roughly estimated from the deformation assuming a purely elastic behavior (47) (Eq. 1; see full line in Fig. 3 B). The fit to the experimental results corresponds to $B = 21$–38 MPa for the diseased SLBs. Comparably, Young's modulus calculated with force mapping for the diseased SLB (30 MPa; Fig. 2 C) falls within the range of the calculated
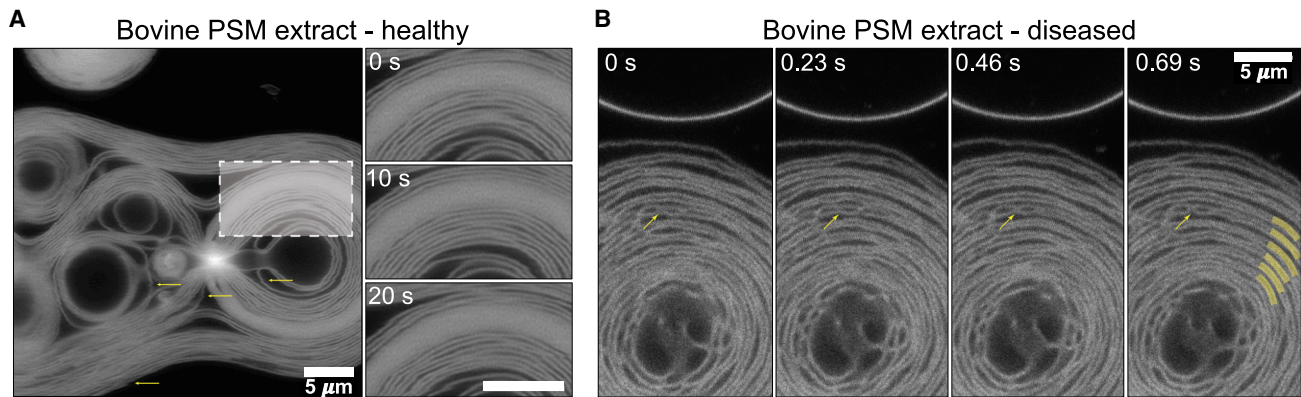
FIGURE 4 Laser scanning confocal microscopy images of bovine PSM extract GMLVs tagged with 0.1 mol % of 1,1′-dioctadecyl-3,3,3′,3′-tetramethy-lindocarbocyanine perchlorate. (A) A large healthy bovine PSM extract GMLV with discrete lamellae is visible, with a denser GMLV in the top left. The region highlighted by a dashed white box is magnified on the right at three time points. The lamellae undulate to maintain a stable inter-bilayer separation. Horizontal arrows point to horizontal jogs that are motion artifacts. (B) A large diseased bovine PSM extract GMLV with discrete lamellae is visible. Lamellae appear to be grouped in pairs but with intermembrane contacts (yellow arrows) that are stable for at least 10 s. Several bilayer pairs are highlighted with thick yellow lines. All images have the same 5 μm scale. To see this figure in color, go online.

bulk modulus from SFA. Finally, a film-thickness transition (Δ_w) with a change in thickness of $\approx 6 \pm 1$ Å was reproducibly measured (Fig. S6), and the transition was reversible upon unloading. Such structural changes likely reflect a rearrangement of lipid domains upon an applied stress, as recently demonstrated for other systems (41).

$$\frac{F}{R} = \pi B \frac{(D - D_B)^2}{D_B} \qquad (1)$$

CL alters PSMs morphology

Fig. 4 shows laser scanning confocal microscopy images of giant multilamellar vesicles (GMLVs) formed from bovine PSM extracts in healthy (no CL) and diseased (with 8 mol % CL) environments. We evaluated the GMLV morphology evolution as as function of time.

In the healthy bovine PSM extract (Fig. 4 A), we observe bilayers individually resolved as well as intense fluorescence emissions from densely packed lamellae that are no longer resolved. Two signs of bilayer motion become apparent in the image. First, motion artifacts within each image appear as horizontal jogs pointed by yellow arrows in Fig. 4 A, which occur because the image is collected by scanning a laser line by line down the image, taking longer exposure times. This is enough for bilayers to move during the scan and create a motion artifact. Second, we tracked the motion over time. Small undulations manifest in the bilayers observed in images taken 10 s apart (Fig. 4 A, right panel), although the average separation does not appear to change. A similar effect is observed in diseased bovine PSMs. A GMLV is observed with its individually resolved bilayers. As time progresses, membrane undulations like those in

the healthy PSM extract are visible, but membranes appear to attract and form interconnected domains (Fig. 4 B, yellow arrows). Two additional distinctive features arise in diseased bovine PSM extracts. First, the lamellae appear to move in pairs. While lamellae undulate in both directions, a noticeably smaller distance between each pair of bilayers is maintained over time. This is consistent with what we previously observed: that CL induces dehydration of pulmonary surfactant multilamellar bodies (13). Second, the points of contact between lamellae are stable over time, which indicates that they consist of stable intermembrane hemifusion contacts.

Membrane fusion in living systems is highly regulated by membrane proteins. Complete fusion and formation of a pore costs considerable elastic energy (48–50), whereas its structural intermediate states, such as stalks and hemifusion contacts, require less energy because no topological transitions occur, so only the bending modulus contributes (51–53). However, additional conditions must be met. First, hemifusion depends on composition. For instance, inverted-conical lipids like CL produce negative contributions to the spontaneous curvature of the proximal membrane monolayers they insert into (Fig. 3 C). This shift increases the tension and locally lowers the bending modulus of the monolayers promoting hemifusion (54–57). Second, hemifusion is facilitated by local dehydration leading to the proximity of apposed bilayers due to osmotic pressure, i.e., two monolayers need to be in close contact to undergo hemifusion (34,56). Fig. 4 B shows that CL leads to smaller interbilayer separation, and we have previously shown that CL decreased the thickness of the water layer separating proximal bilayers in multilamellar PSMs (13). Finally, reorganization of lipid domains is significant for the initial monolayer-monolayer contact. Lipid domains rearrange to decrease the energy barrier of hemifusion (41). We have shown here that CL promotes phase separation in PSMs.

Consequently, CL possesses the properties required to stabilize the formation of stalks and hemifused contacts in diseased lung membranes.

Intermembrane contacts in PSMs are naturally facilitated by surfactant proteins, and possibly PG, and allow oxygen diffusion (58). Moreover, the excess of CL under pathological conditions further promotes hemifusion. We previously demonstrated (14) that increasing the CL concentration in PSMs enhances X-ray diffraction spots corresponding to periodic intermembrane contacts. This results in the significantly enhanced permeation of oxygen (hyperoxia) through PSM bovine extracts and lipid models. Even though enhanced oxygen permeation could be perceived as a positive outcome, it disrupts the gas-exchange balance and leads to hyperoxia, a condition that directly potentiates and aggravates bacterial pneumonia (59,60). During pneumonia, hyperoxia correlates with elevated levels of CL in the PSMs due to an increased number of intermembrane contacts. We have no reasons to expect CL-driven inter-membrane contacts to be structurally (or topologically) distinct from protein-driven ones. Further investigation would elucidate whether CL-driven contacts enable higher translational and local lipid dynamics compared with protein-pinned membranes.

CONCLUSION

Excess CL in lung membranes has been associated with the etiology of lung diseases such as pneumonia. It has been previously suggested that CL locally dehydrates lung membranes, induces domain formation, and promotes the formation of inter-bilayer contacts, i.e., stalks that disrupt gas permeation. In this article, we have studied the structure and elasticity of PSMs. The findings indicate that CL 1) increased the roughness and promoted domain correlation across PSMs, 2) shifted Young's modulus values toward membrane stiffening, and 3) led to long-range attractive inter-bilayer forces and the stabilization of hemifusion contacts between proximal monolayers. Since lung membranes regulate contraction/expansion, i.e., mechanical behavior of the alveoli, the alteration of the structure, elasticity, and inter-membrane interactions induced by pathological factors, such as excess CL, are therefore expected to critically impair PSM behavior. For instance, the effect of CL in membrane elasticity will likely impair breathing as well as surfactant protein binding and hence functionality, resulting in flawed respreading of lung lipids to the air-water interface. Consequently, a deeper understanding of the biophysical roles of the lipidic components of the lung membranes under pathological conditions should enable pathways to develop better therapeutic approaches. Finally, this research also helps to fill the existing gap between our knowledge of mammal lung pathology and the biophysical properties of pulmonary membranes.

SUPPORTING MATERIAL

Supporting material can be found online at https://doi.org/10.1016/j.bpj.2022.02.018.

AUTHOR CONTRIBUTIONS

ACKNOWLEDGMENTS

SUPPORTING CITATIONS

References (61–68) appear in the Supporting Material.

REFERENCES

1. Kahn, M. C., G. J. Anderson, …, S. B. Hall. 1995. Phosphatidylcholine molecular species of calf lung surfactant. *Am. J. Physiol. Lung Cell Mol. Physiol.* 269:L567–L573.

2. Lopez-Rodriguez, E., and J. Pérez-Gil. 2014. Structure-function relationships in pulmonary surfactant membranes: from biophysics to therapy. *Biochim. Biophys. Acta Biomembr.* 1838:1568–1585.

3. Parra, E., and J. Pérez-Gil. 2015. Composition, structure and mechanical properties define performance of pulmonary surfactant membranes and films. *Chem. Phys. Lipids.* 185:153–175.

4. Notter, R. H. 2000. Lung Surfactants, First edition. CRC Press.

5. Andreassen, S., K. L. Steimle, …, D. S. Karbing. 2010. The effect of tissue elastic properties and surfactant on alveolar stability. *J. Appl. Physiol.* 109:1369–1377.

6. Rooney, S. A., S. L. Young, and C. R. Mendelson. 1994. Molecular and cellular processing of lung surfactant. *FASEB J.* 8:957–967.

7. Ray, N. B., L. Durairaj, …, R. K. Mallampalli. 2010. Dynamic regulation of cardiolipin by the lipid pump Atp8b1 determines the severity of lung injury in experimental pneumonia. *Nat. Med.* 16:1120–1127.

8. Israelachvili, J. 2011. Intermolecular and Surface Forces, Third edition. Academic Press.

9. Beltrán-Heredia, E., F.-C. Tsai, …, F. Monroy. 2019. Membrane curvature induces cardiolipin sorting. *Commun. Biol.* 2:1–7.

10. Boyd, K. J., N. N. Alder, and E. R. May. 2018. Molecular dynamics analysis of cardiolipin and monolysocardiolipin on bilayer properties. *Biophys. J.* 114:2116–2127.

11. Renner, L. D., and D. B. Weibel. 2011. Cardiolipin microdomains localize to negatively curved regions of *Escherichia coli* membranes. *PNAS.* 108:6264–6269.

12. Sorre, B., A. Callan-Jones, …, P. Bassereau. 2009. Curvature-driven lipid sorting needs proximity to a demixing point and is aided by proteins. *PNAS.* 106:5622–5626.

13. Steer, D., S. Leung, ..., C. Leal. 2018. The Structure of lung-mimetic multilamellar bodies with lipid compositions relevant in pneumonia. *Langmuir.* 34:7561–7574.

14. Kim, M., M. Porras-Gomez, and C. Leal. 2020. Graphene-based sensing of oxygen transport through pulmonary membranes. *Nat. Commun.* 11:1–10.

15. Heuberger, M. 2001. The extended surface forces apparatus. part I. Fast spectral correlation interferometry. *Rev. Sci. Instrum.* 72:1700–1707.

16. Heuberger, M., J. Vanicek, and M. Zäch. 2001. The extended surface forces apparatus. II. Precision temperature control. *Rev. Sci. Instrum.* 72:3556–3560.

17. Kresse, K. M., M. Xu, ..., A. B. Subramaniam. 2016. Novel application of cellulose paper as a platform for the macromolecular self-assembly of biomimetic giant liposomes. *ACS Appl. Mater. Inter.* 8:32102–32107.

18. Radmacher, M., R. Tillamnn, ..., H. Gaub. 1992. From molecules to cells: imaging soft samples with the atomic force microscope. *Science.* 257:1900–1905.

19. Sennato, S., F. Bordi, ..., S. Rufini. 2005. Evidence of domain formation in cardiolipin- glycerophospholipid mixed monolayers. a thermodynamic and AFM study. *J. Phys. Chem. B.* 109:15950–15957.

20. Heberle, F. A., R. S. Petruzielo, ..., J. Katsaras. 2013. Bilayer thickness mismatch controls domain size in model membranes. *J. Am. Chem. Soc.* 135:6853–6859.

21. Palmieri, V., D. Lucchetti, ..., M. De Spirito. 2015. Mechanical and structural comparison between primary tumor and lymph node metastasis cells in colorectal cancer. *Soft matter.* 11:5719–5726.

22. Lopez, J. I., I. Kang, ..., V. M. Weaver. 2011. In situ force mapping of mammary gland transformation. *Integr. Biol.* 3:910–921.

23. Norman, M. D., S. A. Ferreira, ..., E. Gentleman. 2021. Measuring the elastic modulus of soft culture surfaces and three-dimensional hydrogels using atomic force microscopy. *Nat. Protoc.* 16:2418–2449.

24. Picas, L., F. Rico, and S. Scheuring. 2012. Direct measurement of the mechanical properties of lipid phases in supported bilayers. *Biophys. J.* 102:L01–L03.

25. Boscia, A. L., B. W. Treece, ..., S. Tristram-Nagle. 2014. X-ray structure, thermodynamics, elastic properties and MD simulations of cardiolipin/dimyristoylphosphatidylcholine mixed membranes. *Chem. Phys. Lipids.* 178:1–10.

26. Zhou, J., D. Liang, and S. Contera. 2015. Effect of intra-membrane C 60 fullerenes on the modulus of elasticity and the mechanical resistance of gel and fluid lipid bilayers. *Nanoscale.* 7:17102–17108.

27. Evans, D. F., and H. Wennerström. 1999. The Colloidal Domain: Where Physics, Chemistry, Biology, and Technology Meet, Second edition. Wiley-Vch New York, p. 672.

28. Keating, E., L. Rahman, ..., N. O. Petersen. 2007. Effect of cholesterol on the biophysical and physiological properties of a clinical pulmonary surfactant. *Biophys. J.* 93:1391–1401.

29. Leonenko, Z., E. Finot, ..., M. Amrein. 2006. Effect of cholesterol on the physical properties of pulmonary surfactant films: atomic force measurements study. *Ultramicroscopy.* 106:687–694.

30. Róg, T., H. Martinez-Seara, ..., I. Vattulainen. 2009. Role of cardiolipins in the inner mitochondrial membrane: insight gained through atom-scale simulations. *J. Phys. Chem. B.* 113:3413–3422.

31. Unsay, J. D., K. Cosentino, ..., A. J. García-Sáez. 2013. Cardiolipin effects on membrane structure and dynamics. *Langmuir.* 29:15878–15887.

32. Dahlberg, M., and A. Maliniak. 2008. Molecular dynamics simulations of cardiolipin bilayers. *J. Phys. Chem. B.* 112:11655–11663.

33. Poyry, S., T. Rog, ..., I. Vattulainen. 2009. Mitochondrial membranes with mono-and divalent salt: changes induced by salt ions on structure and dynamics. *J. Phys. Chem. B.* 113:15513–15521.

34. Aeffner, S., T. Reusch, ..., T. Salditt. 2009. Membrane fusion intermediates and the effect of cholesterol: an in-house X-ray scattering study. *Eur. Phys. J. E.* 30:205–214.

35. Chavarha, M., R. W. Loney, ..., S. B. Hall. 2015. Hydrophobic surfactant proteins strongly induce negative curvature. *Biophys. J.* 109:95–105.

36. Israelachvili, J. N., and D. Tabor. 1972. The measurement of van der Waals dispersion forces in the range 1.5 to 130 nm. *Proc. R. Soc. London, Ser. A.* 331:19–38.

37. Wong, J. Y., C. K. Park, ..., J. Israelachvili. 1999. Polymer-cushioned bilayers. II. An investigation of interaction forces and fusion using the surface forces apparatus. *Biophys. J.* 77:1458–1468.

38. Banquy, X., K. Kristiansen, ..., J. N. Israelachvili. 2012. Adhesion and hemifusion of cytoplasmic myelin lipid membranes are highly dependent on the lipid composition. *Biochim. Biophys. Acta Biomembr.* 1818:402–410.

39. Helm, C. A., J. N. Israelachvili, and P. M. McGuiggan. 1992. Role of hydrophobic forces in bilayer adhesion and fusion. *Biochemistry.* 31:1794–1805.

40. Leckband, D., C. Helm, and J. Israelachvili. 1993. Role of calcium in the adhesion and fusion of bilayers. *Biochemistry.* 32:1127–1140.

41. Lee, D. W., K. Kristiansen, ..., J. N. Israelachvili. 2015. Real-time intermembrane force measurements and imaging of lipid domain morphology during hemifusion. *Nat. Commun.* 6:1–8.

42. Rosenberg, K. J., J. L. Ross, ..., J. Israelachvili. 2008. Complementary dimerization of microtubule-associated tau protein: implications for microtubule bundling and tau-mediated pathogenesis. *PNAS.* 105:7445–7450.

43. Espinosa-Marzal, R. M., G. Fontani, ..., R. Crockett. 2013. Sugars communicate through water: oriented glycans induce water structuring. *Biophys. J.* 104:2686–2694.

44. Helm, C., J. Israelachvili, and P. McGuiggan. 1989. Molecular mechanisms and forces involved in the adhesion and fusion of amphiphilic bilayers. *Science.* 246:919–922.

45. Marra, J., and J. Israelachvili. 1985. Direct measurements of forces between phosphatidylcholine and phosphatidylethanolamine bilayers in aqueous electrolyte solutions. *Biochemistry.* 24:4608–4618.

46. Weber, T., B. V. Zemelman, ..., J. E. Rothman. 1998. SNAREpins: minimal machinery for membrane fusion. *Cell.* 92:759–772.

47. Zappone, B., N. J. Patil, ..., G. Lombardo. 2018. Transient viscous response of the human cornea probed with the Surface Force Apparatus. *PLoS One.* 13:e0197779.

48. Chernomordik, L., M. M. Kozlov, and J. Zimmerberg. 1995. Lipids in biological membrane fusion. *J. Membr. Biol.* 146:1–14.

49. Chernomordik, L. V., J. Zimmerberg, and M. M. Kozlov. 2006. Membranes of the world unite. *J. Cell Biol.* 175:201–207.

50. Zimmerberg, J. 2001. How can proteolipids be central players in membrane fusion? *Trends Cell Biol.* 11:233–235.

51. Hu, M., J. J. Briguglio, and M. Deserno. 2012. Determining the Gaussian curvature modulus of lipid membranes in simulations. *Biophys. J.* 102:1403–1410.

52. Khattari, Z., S. Köhler, ..., T. Salditt. 2015. Stalk formation as a function of lipid composition studied by X-ray reflectivity. *Biochim. Biophys. Acta Biomembr.* 1848:41–50.

53. Yang, L., and H. W. Huang. 2002. Observation of a membrane fusion intermediate structure. *Science.* 297:1877–1879.

54. Siegel, D. P. 1993. Energetics of intermediates in membrane fusion: comparison of stalk and inverted micellar intermediate mechanisms. *Biophys. J.* 65:2124–2140.

55. Chernomordik, L. V., and M. M. Kozlov. 2005. Membrane hemifusion: crossing a chasm in two leaps. *Cell.* 123:375–382.

56. Chernomordik, L. V., and M. M. Kozlov. 2008. Mechanics of membrane fusion. *Nat. Struct. Mol. Biol.* 15:675–683.

57. Kozlovsky, Y., and M. M. Kozlov. 2002. Stalk model of membrane fusion: solution of energy crisis. *Biophys. J.* 82:882–895.

58. Olmeda, B., L. Villén, ..., J. Perez-Gil. 2010. Pulmonary surfactant layers accelerate O2 diffusion through the air-water interface. *Biochim. Biophys. Acta Biomembr.* 1798:1281–1284.

59. Crouse, D., G. Cassell, …, G. Cassady. 1990. Hyperoxia potentiates Ureaplasma urealyticum pneumonia in newborn mice. *Infect. Immun.* 58:3487–3493.

60. Tateda, K., J. C. Deng, …, T. J. Standiford. 2003. Hyperoxia mediates acute lung injury and increased lethality in murine Legionella pneumonia: the role of apoptosis. *J. Immunol.* 170:4209–4216.

61. Krieg, M., G. Fläschner, …, D. J. Müller. 2019. Atomic force microscopy-based mechanobiology. *Nat. Rev. Phys.* 1:41–57.

62. Sicard, D., L. E. Fredenburgh, and D. J. Tschumperlin. 2017. Measured pulmonary arterial tissue stiffness is highly sensitive to AFM indenter dimensions. *J. Mech. Behav. Biomed. Mater.* 74:118–127.

63. Terzi, M. M., M. Deserno, and J. F. Nagle. 2019. Mechanical properties of lipid bilayers: a note on the Poisson ratio. *Soft matter.* 15:9085–9092.

64. Schrader, A. M., S. H. Donaldson, …, J. N. Israelachvili. 2015. Correlating steric hydration forces with water dynamics through surface force and diffusion NMR measurements in a lipid–DMSO–H2O system. *PNAS.* 112:10708–10713.

65. Israelachvili, J. N., and R. M. Pashley. 1983. Molecular layering of water at surfaces and origin of repulsive hydration forces. *Nature.* 306:249–250.

66. Israelachvili, J., and H. Wennerström. 1996. Role of hydration and water structure in biological and colloidal interactions. *Nature.* 379:219–225.

67. Donaldson, S. H., C. T. Lee, …, J. N. Israelachvili. 2011. General hydrophobic interaction potential for surfactant/lipid bilayers from direct force measurements between light-modulated bilayers. *PNAS.* 108:15699–15704.

68. Wilson, B. A., A. Ramanathan, and C. F. Lopez. 2019. Cardiolipin-dependent properties of model mitochondrial membranes from molecular simulations. *Biophys. J.* 117:429–444.

Supplemental information

Pathological cardiolipin-promoted membrane hemifusion stiffens pulmonary surfactant membranes

Marilyn Porras-Gómez, Tooba Shoaib, Dylan Steer, Rosa Maria Espinosa-Marzal, and Cecília Leal

S1 TOPOGRAPHY AND SURFACE ROUGHNESS

Height-phase AFM maps with average surface roughness S_q of healthy (DPPC:DOPG 3:1, molar ratio) and diseased (+ CL 8 mol%) lipid-based PSM models in air at 85-90% RH and room temperature. Average surface roughness Sq was calculated from AFM topography images of area 5 x 5 μm with resolution of 521 x 521 data points (Table S1), using the discrete approximation of the root mean square (RMS), namely

$$S_q = \left[\frac{1}{L} \int_0^L Z(x)^2 dx \right]^{\frac{1}{2}} \approx \left[\frac{1}{N} \sum_{i=1}^{N} Z_i^2 \right]^{\frac{1}{2}} \tag{S.1}$$

where L is the evaluation length, $Z(x)$ is the profile height function at x, N is the number of samples and Z_i is a sample of the profile height function.
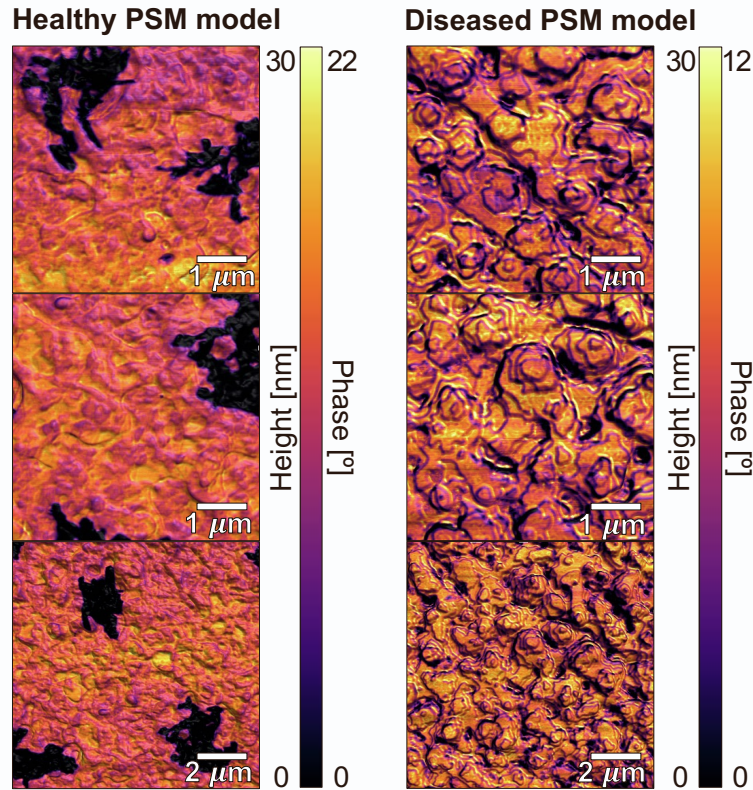

Figure S1: **AFM height-phase maps of the lipid-based PSM models**

Sample	Sq (nm)	SD (nm)	area (μm^2)	data points	n
Healthy PSM SLM	4.9	0.4	25	262144	2
Diseased PSM SLM	7.7	0.4	25	262144	2

Table S1: Average surface roughness

S2 STATISTICS OF FORCE MAP ANALYSIS

Force spectroscopy analysis at room temperature involved recording up to 5 different 5 μm x 5 μm or 1 μm x 1 μm force maps over 128 points x 128 lines (16384 data points) or 95 points and 256 lines (24576 data points). Measurements of Young's modulus E for the supported lipid multilayers (SLM) of bovine pulmonary surfactant membrane (PSM) extract in healthy (no cardiolipin (CL)) and diseased (with 8 mol% CL), and SLM of PSM model in healthy and diseased conditions were performed in air at 85-90% RH. While measurements of on supported lipid bilayers (SLB) of the model were performed in water.

Sample	Data Points	Adj. R2 (Gauss)	Mean E (MPa)	FWHM
Healthy bovine PSM	24576	0.966	32	9
Diseased bovine PSM	16384	0.994	90	30
Healthy PSM model	24576	0.995	41	8
Diseased PSM model	16384	0.974	51	29
Healthy SLB PSM model	16384	0.981	18	15
Diseased SLB PSM model	16384	0.957	30	22

Table S2: Statistics of force map analysis

S3 ANALYSIS OF ELASTICITY MEASUREMENTS

All reported Young's modulus E values result from the peak of a Gaussian fit of the elasticity distribution obtained from the respective force maps. The approximate value of E was calculated from the approaching curves by using the Hertz model for conical tips (Sneddon model) (1, 2):

$$E = \frac{\pi}{2} \frac{(1 - \nu^2)}{tan(\theta)\delta^2} F \tag{S.2}$$

where F is the force of the tip that leads to an indentation depth δ in the sample with an angle θ, $\nu = 0.5$ is the Poisson ratio of lipids (3).
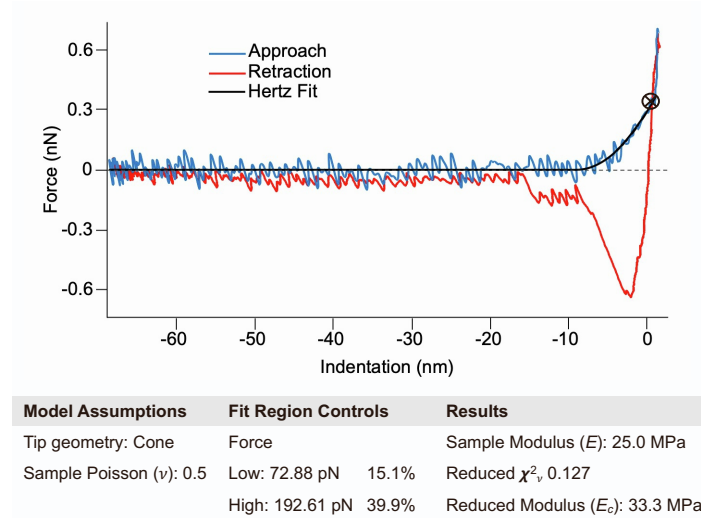

Model Assumptions	Fit Region Controls		Results
Tip geometry: Cone	Force		Sample Modulus (E): 25.0 MPa
Sample Poisson (ν): 0.5	Low: 72.88 pN	15.1%	Reduced χ^2_ν, 0.127
	High: 192.61 pN	39.9%	Reduced Modulus (E_c): 33.3 MPa

Figure S2: **Hertzian fitting. Example of experimental force-indentation curve of the lipid healthy PSM model and the data fitting parameters. Typically, the fitting was of 40% of force**
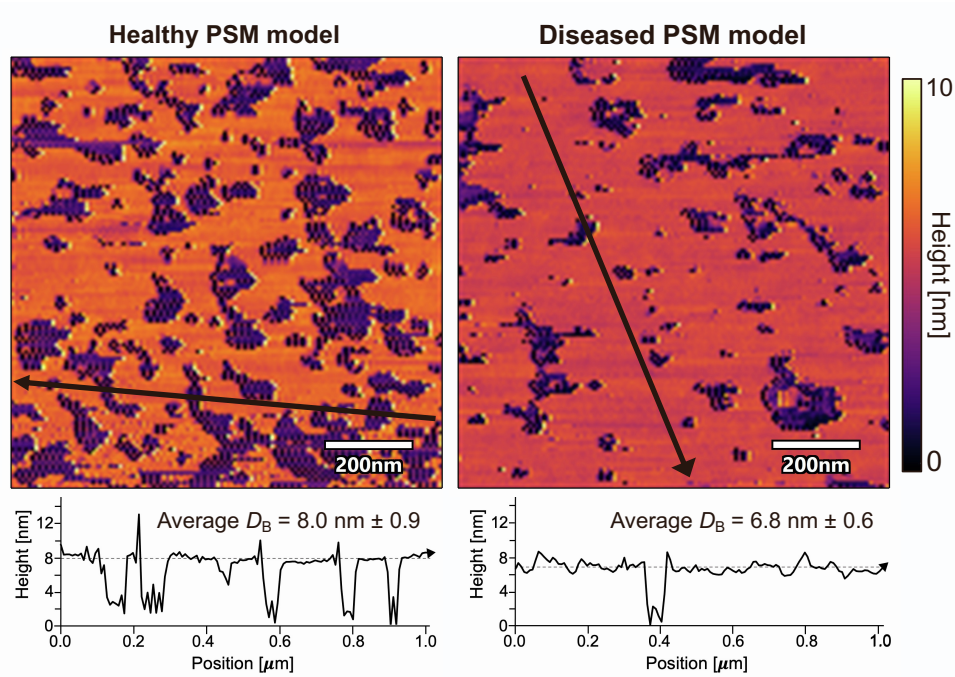
.

S4 THICKNESS OF SUPPORTED LIPID BILAYERS

Figure S3: **Bilayer thickness. The thickness of supported lipid bilayers (SLB) was determined by AFM-in fluid topography. Purple areas correspond to uncovered SiO$_2$ substrates and yellow-orange areas correspond to one supported lipid bilayer. We report average bilayer thickness D_B with standard deviation for healthy and diseased PSM lipid models. We calculated D_B by measuring 8 cross-section lines of 3 different AFM images giving $n = 24$ per sample (healthy and diseased).**

S5 VALUES OF STRETCH K_A AND BENDING MODULUS κ_C

Sample	K_A (pN/nm)	κ_C (k$_B$$T$)
Healthy bovine PSM	341	160
Diseased bovine PSM	960	450
Healthy PSM model	437	205
Diseased PSM model	544	255
Healthy SLB PSM model	192	90
Diseased SLB PSM model	320	150

Table S3: Calculated K_A and κ_C
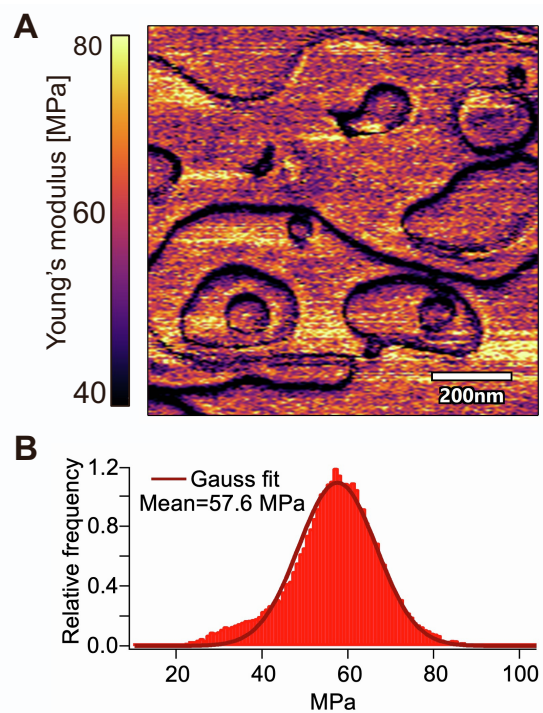
S6 EFFECT OF CHOLESTEROL ON THE PSM MODEL

Figure S4: **Healthy SLM of PSM model with cholesterol. Preliminary data of Young's modulus map of healthy system containing 15 mol% cholesterol (A) and its corresponding Young's modulus distribution (B).**

S7 MODEL FOR INTERMEMBRANE FORCES

$$W = W_{\text{DLVO}} + W_{\text{ster}} + W_{\text{hyd}} + W_{\text{agg}} \tag{S.3}$$

The model (Eq. S.3) accounts for the most important inter- and intramolecular interactions in lipid bilayers used to calculate the energy potential E, which is related to the interaction energy per unit area through $W = E/a$; a is the lipid area. In SFA experiments, we measure F, the interbilayer force, which is related to the interaction energy W by the Derjaguin approximation: $W = F/2\pi R$, R being the radius of curvature of the mica surfaces ($R = 2$ cm). Intermembrane forces include van der Waals (vdW), electrical double-layer, short range (repulsive) hydration and (attractive) hydrophobic forces (4, 5). DLVO theory accounts well for electrical double-layer (EDL) forces and vdW attractive forces but cannot predict bilayer fusion. At interbilayer distances ($d \lesssim$ 1-3 nm), a strong repulsion consisting of steric (hydration) forces and undulation forces dominates over the DLVO force. The steric hydration force exponentially decays with d ($E_{\text{ster}} = C_{\text{ster}} exp(-d/D_{\text{ster}})$), with a decay length D_{ster} of the order of the hydration shell of the hydrophilic headgroups (typical range 0.2–1 nm) (6). Alternatively, steric hydration forces have been modeled by Alexander-de Gennes theory (7), i.e., assuming the headgroups' thermal fluctuations in a good solvent behave like a polymer brush. Due to their short-ranged nature, steric hydration forces were originally considered to stem from water structuring (8). Further studies revealed its entropic origin (9), which arises from the overlap of protrusions and hydrated headgroups. Here, we used the first and most simple approach. Steric hydration forces are thus influenced by the extent of lipid protrusion and the size of the hydrated headgroups, and hence, by their hydration strength. We assumed $D_{\text{ster}} = 0.9nm$, as in previous (6), while C_{ster} is a fitting parameter. On the other hand, longer-range undulation forces W_{und} arise from the confinement of the bilayer ripples (undulations). Hence, the bending modulus of the lipid bilayers, which is mostly affected by the phase of the lipids, is a key property affecting W_{und}. The phase of the lipid domains depends on the length of the tail and its saturation, headgroup type, and temperature. However, W_{und} is only significant when the lipid bilayers are "free-standing" and "unstressed." This can happen if bilayers are deposited on "polymer cushions" but a solid substrate like mica is known to suppress undulation forces. Finally, an empiric model has been proposed for the hydrophobic force between bilayers (6). For lipids in a liquid-like state, which can be easily deformed or depleted by applying stresses, the hydrophobic energy potential is given by $E_{\text{hyd}} = -\gamma(a - a_0)exp(-d/D_{\text{hyd}})$, where $a = a_0(1 - exp(-d/D_{\text{hyd}}))^{-1/2}$, D_{hyd} the decay length, γ the interfacial energy, and a and a_0 stressed and unstressed molecular areas, respectively. For bilayers in gel state, a is a weaker function of d due to their larger elastic modulus. The model also accounts for the self-aggregation energy between tails $E_{\text{agg}} = 2\gamma a_0 + \gamma/a(a - a_0)^2$ (6), which includes the elastic deformation of the bilayer, headgroup repulsions and the surface tension. To directly compare the experiments $W_{\text{exp}} = F/(2\pi R)$ with the model, the energy is referenced to the energy at $d = \infty$, i.e., $W(d) - W(\infty)$.

The model was first fit only at large separations ($D > 20$ nm), where only the electrical double layer force is relevant, and other contributions in Eq. S.3 can be neglected. Hence, the long–range surface force is fit by the DLVO model, which gives the DLVO force as the sum of van der Waals F_{VDW} and electric double layer forces F_{EDL}:

$$\frac{F_{\text{DLVO}}}{R} = \frac{F_{\text{VDW}}}{R} + \frac{F_{\text{EDL}}}{R} = -\frac{A_{\text{H}}}{6D^2} + 4\pi\varepsilon\varepsilon_0\kappa\phi_0^2 exp(-\kappa D) \tag{S.4}$$

A_{H} being the Hamaker constant ($1.966x10^{-20}J$), D the separation between mica surfaces, $R_{\text{eff}} = R$ the radius of the surface ($R = 2cm$), κ the inverse of the Debye length $\kappa = 1/\lambda_{\text{EDL}}$, ϕ_0 the surface potential, ε the relative permittivity of the solution (unitless) and ε_0 the vacuum permittivity. The expression for the EDL force assumes constant surface potential. It is important to emphasize, that the expression for the EDL force was derived from a linearization of the Poisson-Boltzman equation that is only strictly valid for small potentials (<25 mV). The errors introduced by this linearized approach are typically not excessive for potentials as high as 200 mV, except for distances that are significantly shorter than one Debye length. The fitting parameters are the Debye length and the surface potential, which are determined to be $\lambda_{\text{EDL}} \approx 28.7 \pm 3.0nm$ and $\phi_0 \approx 106 \pm 25mV$ in good approximation. The Debye length corresponds to an ionic strength in a 1:2 electrolyte of 0.038 ± 7 mM, while the ionic strength of the 0.15 mM lipid solution with 8 mol% cardiolipin is 0.036 mM.

To determine the percentage of charged cardiolipin in the membrane that is responsible for the surface potential determined from surface force measurements, the following expression was used:

$$\approx \frac{\sigma e_{\text{c}} a_0}{X_z} \tag{S.5}$$

σ being the surface charge of the diseased membrane, $z = 2$ the number of charges per CL molecule, the electron charge $e_c = 1.6x10^{-19}C$, and X gives the percentage of CL in the membrane, which is assumed to be 8 mol%, as the CL in the lipid solution. The parameter a_0 is taken as the unstressed average area per lipid molecule in the bilayer. We assume a value of $a_0 \approx 67\text{Å}^2$, which is in the range of the reported values for DPPC with 7 mol% CL (10). This value considers that the presence of CL in the membrane increases the area per lipid molecule. The Grahame equation was used to roughly estimate the charge σ of an isolated membrane surface (11). Note that in our experiment, we measure the intermembrane interaction when we approach the surfaces against each other, and hence, the model does not strictly apply to the conditions of the experiment, but it enables us to estimate the order of magnitude of the surface charge. For a 1:2 electrolyte,

$$\sigma^2 = 2\varepsilon\varepsilon_0 kTC_\infty (exp(2e\phi_0/kT) + 2exp(-e\phi_0/kT) - 3)^2 \tag{S.6}$$

This yields $\sigma \approx -63.6 \pm 3.5C/cm^2$ and $17 \pm 1\%$ is the estimated number of dissociated CL molecules in the membrane. In a few experiments we calculated a much larger surface charge corresponding to $85 \pm 10\%$ dissociated CL molecules in the bilayer.

To determine the interfacial energy, Eq. S.3 was fit to the experimental results, using the known parameters for the DLVO contribution. For the decay lengths of the steric and hydrophobic terms, we have taken $D_{hyd} = 1.2nm$ and $D_{ster} = 0.9nm$, within the typical range for these decay lengths (6). The parameters of interfacial tension γ and C_{ster} were used as the fitting parameters. This yields $C_{ster} = 0.41 \pm 0.14x10^{-20}J$ and γ between 23 and 41 mJ/m^2. Typical values for γ range from 20–50 mJ/m^2 (6).
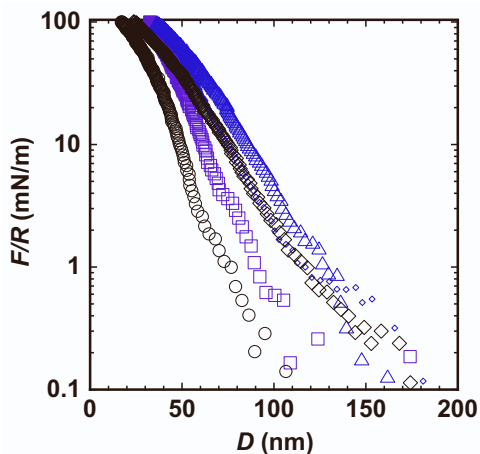
S8   LONG-RANGE FORCES

Figure S5: **Long-range force F vs. D for healthy inter-vesicle forces. A compression up to 100 mN/m does not lead to vesicle fusion in the absence of CL, indicating that the membrane fusion energy is much higher.**

S9   CARDIOLIPIN PROMOTES A STRUCTURAL CHANGE OF THE LIPID MICRODOMAINS UPON COMPRESSION

A film-thickness transition (Δ_w) with a change in thickness of $\approx 0.6 \pm 0.1$ nm was measured and the transition was reversible upon unloading. Such structural changes could reflect a rearrangement of lipid domains upon an applied stress, as recently demonstrated for other systems (12). In two additional experiments (e.g. green curve in Fig. S6), this structural transition did not happen upon the same range of compressions, perhaps suggesting that the composition of the compressed bilayers was different upon reformation.
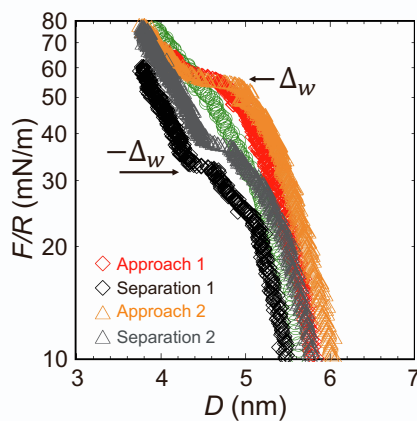

Figure S6: **Reversible structural transition upon compression of the bilayer approach (loading, orange, red, green) and separation (unloading, black and grey). The green circles could correspond to a different bilayer composition.**

S10 SUPPORTING REFERENCES

1. Krieg, M., G. Fläschner, D. Alsteens, B. M. Gaub, W. H. Roos, G. J. Wuite, H. E. Gaub, C. Gerber, Y. F. Dufrêne, and D. J. Müller, 2019. Atomic force microscopy-based mechanobiology. *Nat Rev Phys* 1:41–57.

2. Sicard, D., L. E. Fredenburgh, and D. J. Tschumperlin, 2017. Measured pulmonary arterial tissue stiffness is highly sensitive to AFM indenter dimensions. *J Mech Behav Biomed Mater.* 74:118–127.

3. Terzi, M. M., M. Deserno, and J. F. Nagle, 2019. Mechanical properties of lipid bilayers: A note on the Poisson ratio. *Soft matter* 15:9085–9092.

4. Helm, C., J. Israelachvili, and P. McGuiggan, 1989. Molecular mechanisms and forces involved in the adhesion and fusion of amphiphilic bilayers. *Science* 246:919–922.

5. Helm, C. A., J. N. Israelachvili, and P. M. McGuiggan, 1992. Role of hydrophobic forces in bilayer adhesion and fusion. *Biochemistry* 31:1794–1805.

6. Donaldson, S. H., C. T. Lee, B. F. Chmelka, and J. N. Israelachvili, 2011. General hydrophobic interaction potential for surfactant/lipid bilayers from direct force measurements between light-modulated bilayers. *PNAS* 108:15699–15704.

7. Schrader, A. M., S. H. Donaldson, J. Song, C.-Y. Cheng, D. W. Lee, S. Han, and J. N. Israelachvili, 2015. Correlating steric hydration forces with water dynamics through surface force and diffusion NMR measurements in a lipid–DMSO–H2O system. *PNAS* 112:10708–10713.

8. Israelachvili, J. N., and R. M. Pashley, 1983. Molecular layering of water at surfaces and origin of repulsive hydration forces. *Nature* 306:249–250.

9. Israelachvili, J., and H. Wennerström, 1996. Role of hydration and water structure in biological and colloidal interactions. *Nature* 379:219–225.

10. Wilson, B. A., A. Ramanathan, and C. F. Lopez, 2019. Cardiolipin-dependent properties of model mitochondrial membranes from molecular simulations. *Biophys. J.* 117:429–444.

11. Israelachvili, J., 2011. Intermolecular and Surface Forces. Academic Press, Burlington, MA, USA, third edition.

12. Lee, D. W., K. Kristiansen, S. H. D. Jr., N. Cadirov, X. Banquy, and J. N. Israelachvili, 2015. Real-time intermembrane force measurements and imaging of lipid domain morphology during hemifusion. *Nat. Commun.* 6:1–8.